The NIBLES bivariate luminosity–H I mass distribution function revised using Arecibo follow-up observations

Z. Butcher, W. van Driel, S. Schneider

A&A 642, A175 (2020)
https://doi.org/10.1051/0004-6361/202037711

Astronomy & Astrophysics

The NIBLES bivariate luminosity–HI mass distribution function revised using Arecibo follow-up observations⋆

Z. Butcher[1], W. van Driel[2,3], and S. Schneider[1]

[1] University of Massachusetts, Astronomy Program, 536 LGRC, Amherst, MA 01003, USA
e-mail: zbutcher@nrao.edu
[2] GEPI, Observatoire de Paris, PSL Université, CNRS, 5 Place Jules Janssen, 92190 Meudon, France
[3] USN, Station de Radioastronomie de Nançay, Observatoire de Paris, CNRS/INSU USR 704, Université d'Orléans OSUC, Route de Souesmes, 18330 Nançay, France

Received 12 February 2020 / Accepted 18 May 2020

ABSTRACT

We present a modified optical luminosity–HI mass bivariate luminosity function based on HI line observations from the Nançay Interstellar Baryons Legacy Extragalactic Survey (NIBLES), including data from our new, four times more sensitive follow-up HI line observations obtained with the Arecibo radio telescope. The follow-up observations were designed to probe the underlying HI mass distribution of the NIBLES galaxies that were undetected or marginally detected in HI at the Nançay Radio Telescope. Our total follow-up sample consists of 234 galaxies, and it spans the entire luminosity and color range of the parent NIBLES sample of 2600 nearby ($900 < cz < 12\,000\,\mathrm{km\,s^{-1}}$) SDSS galaxies. We incorporated the follow-up data into the bivariate analysis by scaling the NIBLES undetected fraction by an Arecibo-only distribution. We find the resulting increase in low HI mass-to-light ratio densities to be about 10% for the bins $-1.0 \leq \log\left(\frac{M_{\rm HI}/M_\odot}{L_r/L_\odot}\right) \leq -0.5$, which produces an increased HI mass function (HIMF) low mass slope of $\alpha = -1.14 \pm 0.07$, being slightly shallower than the values of -1.35 ± 0.05 obtained by recent blind HI surveys. Applying the same correction to the optically corrected bivariate luminosity function from our previous paper produces a larger density increase of about 0.5 to 1 dex in the lowest HI mass-to-light ratio bins for a given luminosity while having a minimal effect on the resulting HIMF low mass slope, which still agrees with blind survey HIMFs. This indicates that while low HI-mass-to-light ratio galaxies do not contribute much to the one-dimensional HIMF, their inclusion has a significant impact on the densities in the two-dimensional distribution.

Key words. galaxies: statistics – galaxies: general – galaxies: formation – galaxies: dwarf – radio lines: galaxies

1. Introduction

Understanding the large-scale baryonic mass distribution of the Universe has been one of the longest-standing quests in modern astronomy. The present-day baryonic mass distribution provides insight into many different aspects of the evolution of the Universe as it is the current endpoint for all evolutionary models. This included but is not limited to, the evolution of dark matter haloes, how galaxies process gas within galaxies, stellar evolution and heavy element production, and galaxy mergers and interactions. The spatial distribution of dark matter haloes is traced by galaxies whose sizes and morphologies provide constraints on the physical processes undergone by the baryons.

The most common and widely used quantifier of the galaxy population has historically been the optical luminosity function (LF), which describes the volume density of galaxies as a function of luminosity (see, e.g., Loveday et al. 1992, 2015; Marzke et al. 1994; Norberg et al. 2002; Blanton et al. 2003; Montero-Dorta & Prada 2009; Geller et al. 2012; McNaught-Roberts et al. 2014; Parsa et al. 2016; Lan et al. 2016). Since the LF is a fundamental tracer of the galaxy population, it is commonly used as a test for semi-analytic galaxy formation models (see, e.g., White & Frenk 1991; Katz et al. 1992; Kauffmann et al. 1993; Cole et al. 1994, 2000; Somerville & Primack 1999; Pearce et al. 2001; Benson et al. 2003; Cooray & Milosavljević 2005).

Similar to the optical LF, the HI mass function (HIMF) has also been used to trace the galaxy population, although to a somewhat lesser extent (see, e.g., Zwaan et al. 1997, 2003; Schneider et al. 1998; Kovac et al. 2005; Springob et al. 2005; Martin et al. 2010; Hoppmann et al. 2015). While both of these population tracers are used as tests of semi-analytic models, they both only trace a single dimension of the galaxy population.

The optical luminosity–HI mass bivariate luminosity function (BLF) describes the volume density of galaxies as a function of both their luminosity and HI mass. When integrated over all luminosities in each HI mass bin, it becomes the HIMF, and when integrated over all HI masses in each luminosity bin, it becomes the optical LF. The advantage of analyzing the galaxy population in more than one dimension simultaneously is that it provides details on the distribution of one variable as a function of the other, allowing for finer tuning of formation models.

Previously, Lemonias et al. (2013) presented a bivariate distribution as a function of stellar and HI masses. However it was essentially stellar mass folded into a one-dimensional HIMF and it covered a far smaller mass range than our sample.

The Nançay Interstellar Baryons Legacy Extragalactic Survey (NIBLES), being an optically selected survey, is able to probe HI masses to lower levels than typical blind HI surveys

⋆ Tables A.1 and A.2, along with the Hi line spectra are only available at the CDS via anonymous ftp to cdsarc.u-strasbg.fr (130.79.128.5) or via http://cdsarc.u-strasbg.fr/viz-bin/cat/J/A+A/642/A175

due to increased on-source integration times. This provides the advantage of being able to probe HI mass distributions as a function of optical luminosity much better than blind HI surveys, which have no optical selection criteria. Conversely, blind HI surveys tend to contain more HI rich, low surface brightness (LSB) galaxies, which are often difficult to detect or completely absent from optical surveys. The practical implications of these selection criteria are that HIMFs from optically selected sources tend to have flatter slopes than their blind survey counterparts (see, e.g., Rao & Briggs 1993). However, for the purposes of constructing a BLF, the HI distribution as a function of luminosity is the critical component and is more readily obtained from optical selection criteria.

In Butcher et al. (2018, hereafter Paper III), we present the first optical luminosity–HI mass BLF and HIMF of the NIBLES sample of 2600 galaxies selected from the Sloan Digital Sky Survey (SDSS; see, e.g., York et al. 2000) within the local universe ($900 \leq cz \leq 12\,000\,\mathrm{km\,s^{-1}}$). The galaxies were chosen with the goal of obtaining nearly equal numbers of galaxies in each absolute magnitude bin, so that the optical luminosity function was sampled more uniformly than in magnitude-limited studies or blind HI surveys. The project was based on uniform HI-line observations carried out with the 100 m class Nançay Radio Telescope (NRT).

The Nançay observations had a detection rate of 63%, that is, 1497 out of the 2364 target sources for which usable HI spectra were obtained and which were not clearly confused by another galaxy within the telescope beam (van Driel et al. 2016, hereafter Paper I). The undetected galaxies are mainly high-luminosity, gas-poor red objects, and low-luminosity, predominantly blue, galaxies (see also Paper III). Although the low HI mass sources within a given luminosity bin have very little impact on the overall distribution of the one-dimensional HIMF (see Butcher et al. 2018), they do alter the two-dimensional BLF distribution based on both optical luminosity and HI mass.

We identified trends in the HI-mass-to-luminosity (gas-to-light hereafter) ratios, $\frac{M_{\rm HI}/M_\odot}{L_r/L_\odot}$, that are consistent over the entire luminosity range of NIBLES, from which we extrapolated volume densities for galaxies with very low luminosities that lie outside the NIBLES selection criteria due to the SDSS magnitudes being generally unreliable for r-band apparent mag >17.77 (a consequence of the SDSS selection criteria chosen to correspond to their desired target density of 90 objects per square degree, see Loveday 2002). The resulting extrapolated distributions produce a BLF from which we can derive an HIMF that is consistent with blind HI survey HIMFs.

To better understand the properties of the galaxies undetected at Nançay and assess their impact on the BLF, we obtained four times higher sensitivity follow-up observations with the 305 m Arecibo radio telescope. In two earlier Arecibo follow-up campaigns (see Butcher et al. 2016, Paper II, for details) a total of 92 NIBLES galaxies were observed, from a random subsample and a subsample of nearby ($cz < 4000\,\mathrm{km\,s^{-1}}$) blue galaxies with a color $u - z < 2$ mag. We present here results of a third Arecibo observing campaign of 151 objects (including some repeats from the earlier campaigns) designed to provide a fairly uniform sampling of, collectively, 234 NIBLES galaxies that were either not detected or marginally detected at Nançay.

In Sect. 2 we describe the observed galaxy sample; in Sect. 3 we describe the observation strategy and data reduction procedure; in Sect. 4 we review the methodology used to derive BLFs and HIMFs; in Sect. 5 we compare results including the Arecibo sample to the results of the Nançay only sample; and in Sect. 6 we present our conclusions. Solar luminosities are given in the SDSS r-band, derived from Christopher Willmer's calibrations[1].

2. Sample selection

The larger collecting area of the Arecibo radio telescope allows us to reach lower HI mass limits for undetected NIBLES galaxies within the Arecibo declination range. Not all undetected galaxies could be observed due to telescope time scheduling constraints, so we aimed to expand the set of our earlier Arecibo observations to provide a collective subsample covering the entire NIBLES luminosity range in a fairly uniform manner, with less color bias than our earlier campaigns. In total, about half the undetected galaxies within Arecibo's declination range were observed.

The third, and final, Arecibo HI line follow-up observation sample described here consists of 151 NIBLES galaxies that were observed from July 2016 to February 2017 during a total of 58.5 h of telescope time. 132 of these galaxies were classified as Nançay nondetections and 22 were marginal detections. Of these, 9 were previously observed during the first two follow-up campaigns but resulted in nondetections. They were observed in this campaign with longer integration times, resulting in HI line detections of two sources, 1132 and 1983 (see Paper II for details on the first two campaigns). Since the second campaign targeted blue galaxies ($u - z < 2$ mag) these were excluded in this final campaign, which consists mostly of galaxies with redder colors and at greater distances than those in the previous campaigns. We refer to the combined set of observations from all three campaigns as the Arecibo sample hereafter.

The luminosity and color distributions of the Arecibo sample are shown in Figs. 1 and 2 respectively. The latter shows the lack of a color bias, but the former shows that the Arecibo sample has an almost constant number (~25) of objects per luminosity bin, whereas the ensemble of possible Arecibo targets shows a steady increase with luminosity, from about 30 at $\log(L_r/L_\odot) \sim 7$ to about 90 at $\log(L_r/L_\odot) \sim 11$. The decreased percentage of observed sources at higher luminosities does not detrimentally impact our analysis since our requirement is to have higher sensitivity follow-up observations covering the entire luminosity range that are a fair representation of the overall NIBLES sample. Since our observed sources were only limited by telescope availability, and they fully sample the color distribution shown in Fig. 2, the only impact on our analysis is the magnitude of uncertainty due to sampling errors.

3. Observations and results

The observing strategy of the third campaign is identical to that of our previous two at the Arecibo radio telescope (see Paper II). We used the L-wide receiver and the Wideband Arecibo Pulsar Processor (WAPP) autocorrelator backend with two polarizations, a bandpass of 50 MHz ($10\,600\,\mathrm{km\,s^{-1}}$) and 4096 frequency channels separated by $2.6\,\mathrm{km\,s^{-1}}$. The receiver half power beam width is 3.′5 and the system temperature ranges from 28 to 32 K. Data were taken in standard 5/5 min integration ON/OFF position switching mode. All galaxies were first observed for one 5/5 min cycle, and the weak and nondetections were then repeated depending on available telescope time.

Data were reduced using a combination of Phil Perillat's IDL routines and Robert Minchin's CORMEASURE routine from the Arecibo Observatory. All spectra were Hanning smoothed to a

[1] http://mips.as.arizona.edu/~cnaw/sun_2006.html

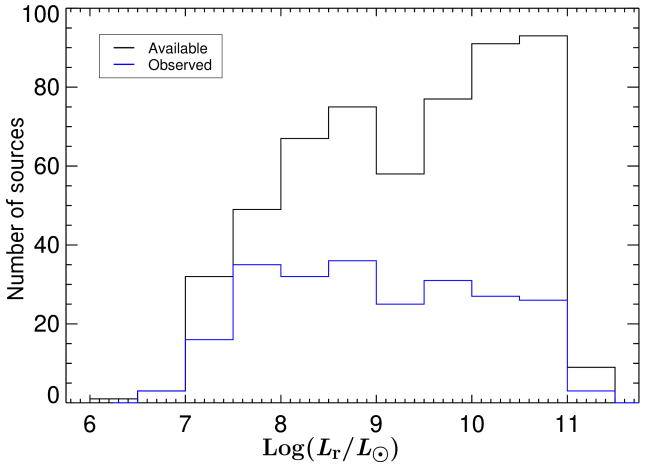

Fig. 1. Luminosity distribution (log($L_r/L_\odot$)) of NIBLES galaxies within the Arecibo declination range that were undetected or marginally detected at Nançay (black), along with the sources that were observed in the Arecibo follow-up campaigns (blue).

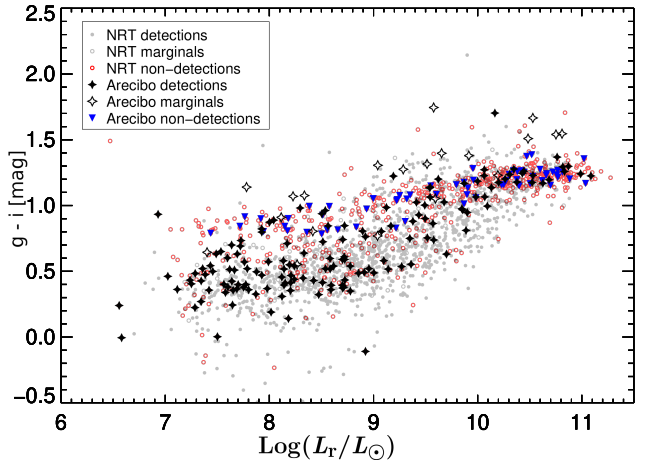

Fig. 2. Integrated $g - i$ color, in mag, as a function of absolute r-band luminosity log($L_r/L_\odot$), both corrected for Galactic extinction following Schlegel et al. (1998). Nançay detections, marginals, and nondetections are represented by gray dots, open gray circles, and open red circles respectively. Arecibo detections, marginals, and nondetections are respectively represented by black solid stars, open stars, and blue downward triangles.

velocity resolution of 18.7 km s^{-1} to match the 18 km s^{-1} resolution of the NRT spectra as closely as possible.

Throughout this paper, all recession velocities given are heliocentric, all HI-line related parameters are according to the conventional optical definition: $V = c(\lambda–\lambda_0)/\lambda_0$, and a Hubble constant of $H_0 = 70$ km s^{-1} Mpc^{-1} is used. Galaxy properties and explanations of derived quantities are listed in Appendix A.

Classification of galaxies into HI detected, nondetected and marginal categories was determined by the three authors, making independent judgments about how each galaxy should be classified based on visual inspection of the HI spectra, with the final adjudication based on a majority consensus. Visual inspection was used rather than a uniform cut in signal-to-noise ratio because the optical redshift of each galaxy was known beforehand, allowing better recognition of source signals.

Color images along with HI line spectra of all 151 galaxies in the third campaign are shown in Appendix A, in Fig. A.1, along with Tables A.1–A.3 listing data for clear detections, marginal detections and nondetections, respectively.

Six sources had unreliable SDSS photometry or were confused by another galaxy within the Arecibo telescope beam (Nos. 0492, 0538, 0748, 0987, 2356 and 2483); these are flagged accordingly in Col. 1 of Tables A.1–A.3. Excluding these six leaves 228 sources to be used for further analysis. Of these, 64% were clearly detected, and 8% marginally detected. The detection fraction depends on color: all of the Arecibo marginal and nondetections are on the redder end of the color distribution ($g - i > 0.8$), Fig. 2.

4. L_r–$M_{\rm HI}$ bivariate luminosity function and HI mass function

The basic methodology we use to derive an L_r–$M_{\rm HI}$ BLF is the same as in Paper III. For each luminosity bin, we first count the number of galaxies in each HI mass bin to determine the HI mass distribution, and then scale the results to obtain the volume density required to match the known luminosity function from Montero-Dorta & Prada (2009). This gives us the two-dimensional volume density as a function of both HI mass and luminosity.

In Paper III we derived an uncorrected bivariate L_r–HI mass distribution using Nançay detections only, and a corrected distribution based on observed trends in the $M_{\rm HI}/L_r$ distribution as a function of luminosity, which we used to extrapolate the distribution down to luminosities well below those of the NIBLES sample galaxies. For the new analysis presented here, which includes our Arecibo follow-up data, we consider only the uncorrected distribution and we treat marginal Arecibo detections as nondetections.

The Arecibo sample provides a fairly uniform subset of undetected NIBLES galaxies within the Arecibo telescope's more limited declination range. Therefore, we can assume that the L_r–HI mass distribution present in the Arecibo sample is a fair representation of all the Nançay undetected galaxies.

We characterize the Arecibo sample's L_r–HI mass distribution in the same manner as for the Nançay sample. To do this, we follow the same general method outlined in Paper III, at first using only the Arecibo data. Specifically, we generate a distribution:

$$\theta_{A\,jk}\Delta M\Delta L = n_{A\,jk}/N_k, \quad (1)$$

where $\theta_{A\,jk}$ represents the distribution of galaxies in the jth HI mass bin and kth luminosity bin of the Arecibo sample only, $n_{A\,jk}$ is the total number of galaxies in the jk HI mass and luminosity bin, and N_k is the total number of galaxies in luminosity bin k.

To combine this distribution with the Nançay sample distribution (see Paper III), we simply add the Arecibo distribution to the Nançay distribution, scaling all k luminosity bins of the Arecibo distribution by the fraction of undetected galaxies in the corresponding k luminosity bin of the Nançay distribution. The resulting combined distribution is shown in Fig. 3 and the original Nançay-only distribution in Fig. 4, using the same color scale. The difference between the two distributions is shown in Fig. 5.

As with the equivalent Nançay detections-only distribution (Fig. 4), the lowest HI mass bin in Fig. 3 is populated exclusively by partial occupation numbers and therefore has a much lower density than the adjacent bins.

The difference between the two distributions is that the Arecibo observations have increased the density of the BLF

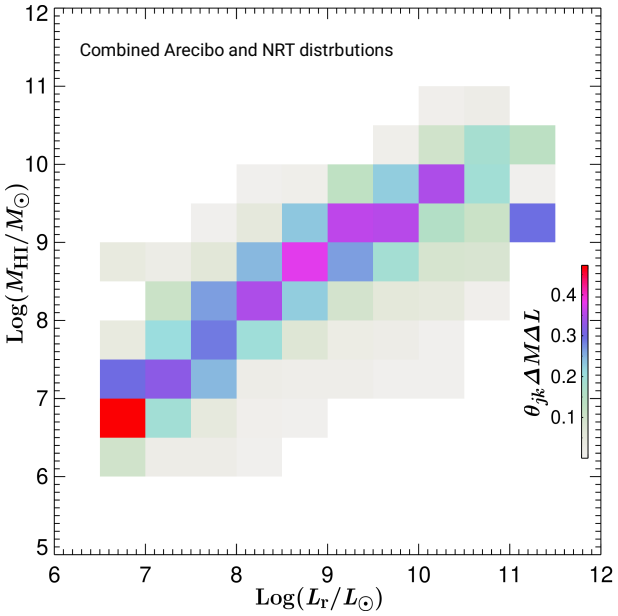

Fig. 3. Two dimensional r-band luminosity–HI mass distribution of the NIBLES sample, derived by combining the scaled two dimensional Arecibo distribution with the Nançay distribution. The color scale indicates the fraction of galaxies that have a particular $\log(M_{HI}/M_\odot)$ for a given $\log(L_r/L_\odot)$, see the legend.

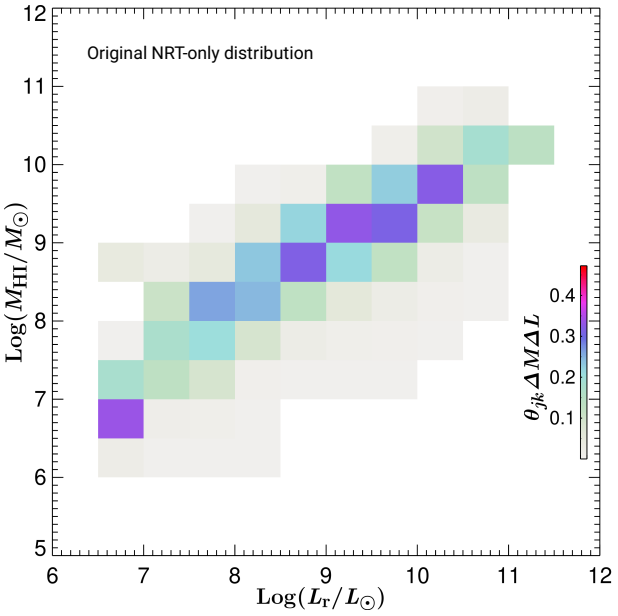

Fig. 4. Two dimensional r-band luminosity–HI mass distribution of the NIBLES sample derived using the Nançay observations only – from Paper III, with the same color scale shown in Fig. 3.

bins by approximately 10% for bins corresponding to the colored regions of Fig. 3. The lower luminosity bins, around $\log(L_r/L_\odot) = 7.25$, show an approximately 20% increase in density and an almost 30% increase for the bin $\log(L_r/L_\odot) = 11.25$, $\log(M_{HI}/M_\odot) = 9.25$.

The $\log(L_r/L_\odot) > 11$ galaxies likely require observations that are even more sensitive than ours at Arecibo to fully sample the HI mass distribution within the 11.25 bin. The $\log(L_r/L_\odot) = 11.25$ bins in the BLF show that bin $\log(M_{HI}/M_\odot) = 9.75$ has a relatively lower density than the two

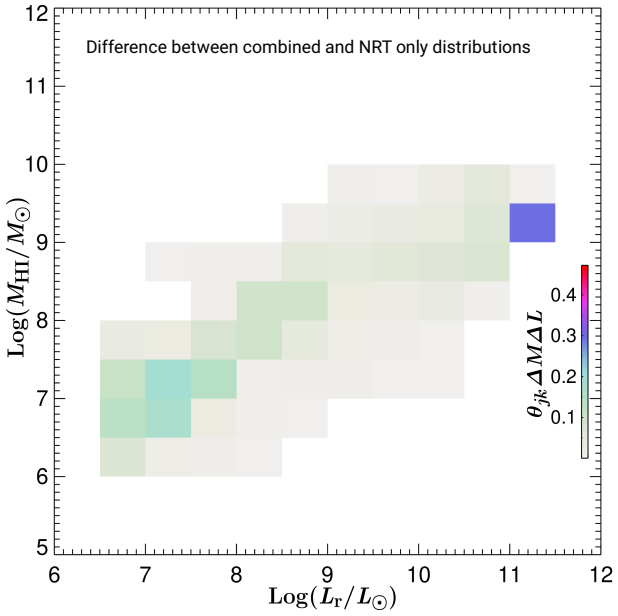

Fig. 5. Difference between Figs. 3 and 4, showing the impact of adding the Arecibo follow-up observations data to the original Nançay data.

adjacent HI mass bins. This is due to insufficient sampling, with the 9.75 bin populated solely by fractional occupation numbers due to the uncertainties in the two adjacent bins. At $\log(L_r/L_\odot) > 11$, the Nançay NIBLES sample contains only 15 galaxies, three of which were detected at Nançay, all within the $\log(M_{HI}/M_\odot) = 10.25$ bin. Of the three Arecibo sample galaxies in the same luminosity bin, the sole detection was in the $\log(M_{HI}/M_\odot) = 9.25$ bin. Using the Arecibo sample as an estimator for the Nançay distribution of undetected HI galaxies leaves the $\log(M_{HI}/M_\odot) = 9.75$ bin populated by only partial occupation numbers based on HI mass uncertainties in the adjacent bins as described in Paper III.

Scaling each luminosity bin from Fig. 3 to the corresponding bin from the Montero-Dorta & Prada (2009) luminosity function (LF) yields the two-dimensional r-band luminosity–HI mass distribution function shown in panel a of Fig. 6, and its corresponding HIMF (panel c). Similarly to Fig. 4 in Paper III, we did not plot the point for the lowest HI mass bin ($\log(M_{HI}/M_\odot) = 6.25$) in the HIMF since it was populated with partial occupation numbers only, due to the relatively high fractional HI mass uncertainty of these sources. The position for the highest HI mass bin ($\log(M_{HI}/M_\odot) = 10.75$) in the HIMF is plotted at the mean value of the measured HI masses contained within the bin rather than at its normal M_{HI} midpoint since this bin is not fully sampled (see Fig. 6).

Values for the mass distribution function from panel a in Fig. 6 are listed in Table 1 as $\log(\Phi(M_{HI},L_r)\Delta M\ \Delta L)$ in units of $\mathrm{Mpc}^{-3}\ \mathrm{dex}^{-1}$ (in solar units), together with their fractional uncertainties.

In Fig. 7 we show the contributions to the HIMF from panel c of Fig. 6 per luminosity bin. Due to the combination of Arecibo and Nançay data, some of the HI mass bins on the extremities of a particular luminosity bin have very large fractional uncertainties, being at or above unity (or above 0.434 on the logarithmic scale). We have omitted these points from the plot for viewing clarity, but their values are listed in Table 1. Additionally, the sole data point in the $\log(L_r/L_\odot) = 11.25$ bin that is below the stated uncertainty threshold is also left off this

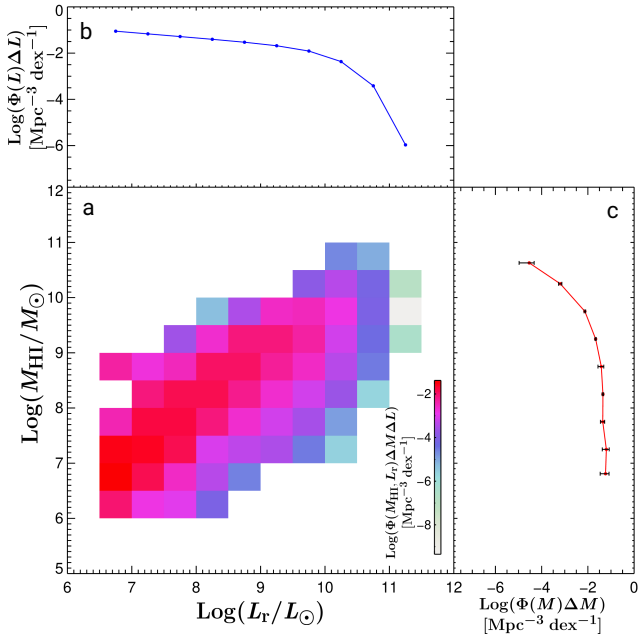

Fig. 6. *Main panel a*: two-dimensional bivariate L_r–HI mass distribution of the NIBLES sample galaxies, derived from a combination of the Nançay and Arecibo sample distributions. The values represented by the colorbar (see the legend) are the volume densities in each 0.5 dex wide bin in both luminosity and HI mass, $\log(\Phi(M_{\rm HI},L_r)\Delta M\Delta L)$ in units of Mpc^{-3} dex^{-1}, as a function of both HI mass and r-band luminosity L_r (in solar units). *Upper panel b*: summation of the main panel over HI mass, which reproduces the input Luminosity Function from Montero-Dorta & Prada (2009), $\log(\Phi(L)\Delta L)$ in units of Mpc^{-3} dex^{-1}. *Right panel c*: summation of the bivariate distribution over luminosity, that is, the HI Mass Function, $\log(\Phi(M)\Delta M)$ in units of Mpc^{-3} dex^{-1}. See the text for further details on the $\log(M_{\rm HI}/M_\odot) = 6.25$ and 10.75 bins in the HIMF.

plot due to its insignificant contribution to the HIMF. Comparing this plot to Fig. 5 in Paper III illustrates that the addition of the Arecibo data to the BLF results in an increased low-HI-mass slope of the HIMF. A Schechter function (see Schechter 1976) fit to this HIMF yields the following parameters:

$$\Phi = 0.012 \pm 0.003,\ \log(M_\star/M_\odot) = 9.63 \pm 0.06,\ \alpha = -1.14 \pm 0.07.$$

The corresponding HIMF based on NRT data only from Paper III yielded the following Schechter fit parameters:

$$\Phi = 0.013 \pm 0.002,\ \log(M_\star/M_\odot) = 9.61 \pm 0.06,\ \alpha = -1.04 \pm 0.07.$$

The addition of the Arecibo data to the Nançay distribution steepens the low-mass slope α, from −1.04 to −1.14, which is expected given the high detection fraction for low luminosity sources in the Arecibo sample. The value of α for the uncorrected combined HIMF is still shallower than the low-mass slopes of blind HI surveys (−1.35 ± 0.05; Zwaan et al. 2005; Haynes et al. 2011) or the −1.26 ± 0.04 of our optically corrected HIMF in Sect. 5.4 of Paper III (which used extrapolated gas-to-light distributions as a function of luminosity to construct distributions in luminosity bins not probed by the NIBLES sample – see also Sect. 5).

In addition to the low-mass slope increase of the HIMF, within each luminosity bin, the density values corresponding to the lowest gas-to-light ratio bins have also increased. We show this effect more clearly in Fig. 8, where we can see that with the exception of the highest luminosity bin, the distributions of the low gas-to-light ratio bins ($\log\left(\frac{M_{\rm HI}/M_\odot}{L_r/L_\odot}\right) \le -0.5$) all display similar shapes and slopes (this was also noted in Fig. 6 of Paper III). The additional detections from the Arecibo sample have increased the population density for the lowest gas-to-light ratios within each luminosity bin by similar amounts, with density increases of about 0.2 dex for $\log\left(\frac{M_{\rm HI}/M_\odot}{L_r/L_\odot}\right)$ values an order of magnitude below the peak, and about 0.4 dex density 1.5 orders of magnitude below the peak.

The largest difference between Fig. 8 and the equivalent Fig. 6 of Paper III is that in Fig. 8, the maximum density values for $\log(L_r/L_\odot) \le 9.25$ all occur in the $\log\left(\frac{M_{\rm HI}/M_\odot}{L_r/L_\odot}\right) = 0$ bin whereas in Fig. 6 of Paper III, descending from $\log(L_r/L_\odot) = 9.25$ to 7.25 there is a progressive increase in the maximum density values from the $\log\left(\frac{M_{\rm HI}/M_\odot}{L_r/L_\odot}\right) = 0$ bin to the 0.5 bin. The new density peaks are the result of adding the relatively lower gas-to-light ratio galaxies detected at Arecibo to the lower luminosity bins. On the other hand, in higher luminosity bins ($\log(L_r/L_\odot) \ge 9.75$) the addition of low gas-to-light ratio objects did not alter the peak $\log(M_{\rm HI}/L_r)$ bins.

The trend in gas-to-light ratios among higher luminosity galaxies is to be expected, and suggests that the more luminous galaxies are more evolved in the sense that they have converted progressively larger fractions of their gas into stars. On the other hand, while the low-luminosity galaxies do not show a shift in their peak gas-to-light ratio, they do display successively larger numbers of galaxies with higher gas fractions at lower luminosities, whereas toward higher luminosities ($\log(L_r/L_\odot) > 9.5$) the higher gas-to-light ratio objects are gradually disappearing.

5. Discussion

In this section we examine how the Arecibo follow-up results (in particular the Arecibo nondetections) relate to the Nançay results, and what we can infer from them about the properties of the NIBLES sample.

Shown in Figs. 9 and 10 are the gas-to-light ratios, $\log\left(\frac{M_{\rm HI}/M_\odot}{L_r/L_\odot}\right)$, plotted as a function of r-band luminosity, L_r, and $g-z$ color respectively. Excluded from the plots are the Nançay data for sources of which Arecibo follow-up observations were obtained, and those that were clearly confused or had unreliable photometry.

It should be noted (see also Paper I) that the estimated upper limits to the HI masses of nondetections are quite conservative, as they are based on the largest observed W_{20} line widths for a given luminosity. For the most luminous sources, which are expected to have the broadest lines, the upper limits tend to be even higher than the NIBLES detections made with the same telescope at the same redshift (see Fig. 9).

The two figures show that: (1) the gas-to-light ratios of the Arecibo nondetections lie below the mean for the Nançay detections for each luminosity, that the mean difference between Arecibo and Nançay nondetections is consistent with the four times higher Arecibo sensitivity, (2) about half of the Arecibo detections lie among the Nançay detections, and the other half have on average about a ten times lower gas-to-light ratio, and (3) all galaxies blueward of $g-z = 0.75$ mag are detected in the Arecibo follow-up observations.

In Paper III we discussed the low-luminosity ($\log(L_r/L_\odot) < 7.25$) galaxies that were missing from the NIBLES sample due to insufficient sensitivity of optical surveys such as the SDSS and the effect this had on the resulting

Table 1. *r*-band luminosity–HI mass distribution function for the uncorrected combined Nançay and Arecibo distribution.

	Log($L_r/L_\odot$)									
$\log\left(\frac{M_{HI}}{M_\odot}\right)$	6.75	7.25	7.75	8.25	8.75	9.25	9.75	10.25	10.75	11.25
	[volume density in Mpc^{-3} dex^{-1}]									
10.75								−4.70 ± 0.42	−5.07 ± 0.20	
10.25							−3.86 ± 0.23	−3.36 ± 0.07	−4.15 ± 0.06	−6.85 ± 0.46
9.75				−5.31 ± 2.27	−3.46 ± 0.23	−2.57 ± 0.07	−2.55 ± 0.05	−2.83 ± 0.04	−4.13 ± 0.11	−9.53 ± 14.39
9.25			−3.62 ± 0.44	−2.69 ± 0.11	−2.16 ± 0.05	−2.13 ± 0.04	−2.36 ± 0.04	−3.17 ± 0.08	−4.37 ± 0.19	−6.50 ± 0.35
8.75	−2.38 ± 1.03	−2.78 ± 0.29	−2.50 ± 0.13	−2.01 ± 0.05	−1.95 ± 0.04	−2.26 ± 0.05	−2.64 ± 0.07	−3.42 ± 0.15	−4.48 ± 0.25	
8.25		−2.13 ± 0.12	−1.86 ± 0.05	−1.86 ± 0.05	−2.16 ± 0.06	−2.71 ± 0.10	−3.15 ± 0.15	−3.70 ± 0.22	−5.59 ± 1.16	
7.75	−2.36 ± 0.85	−1.85 ± 0.10	−1.82 ± 0.06	−2.10 ± 0.07	−2.67 ± 0.13	−3.17 ± 0.21	−3.57 ± 0.29	−4.94 ± 0.76		
7.25	−1.57 ± 0.33	−1.65 ± 0.10	−1.90 ± 0.07	−3.06 ± 0.27	−3.36 ± 0.35	−3.45 ± 0.31	−4.51 ± 0.89	−5.75 ± 2.73		
6.75	−1.39 ± 0.24	−1.88 ± 0.14	−2.59 ± 0.19	−3.43 ± 0.49	−4.61 ± 1.48					

Notes. Volume densities are log($\Phi(M_{HI},L_r)\Delta M\ \Delta L$) in Mpc^{-3} dex^{-1}. The listed uncertainties are fractional.

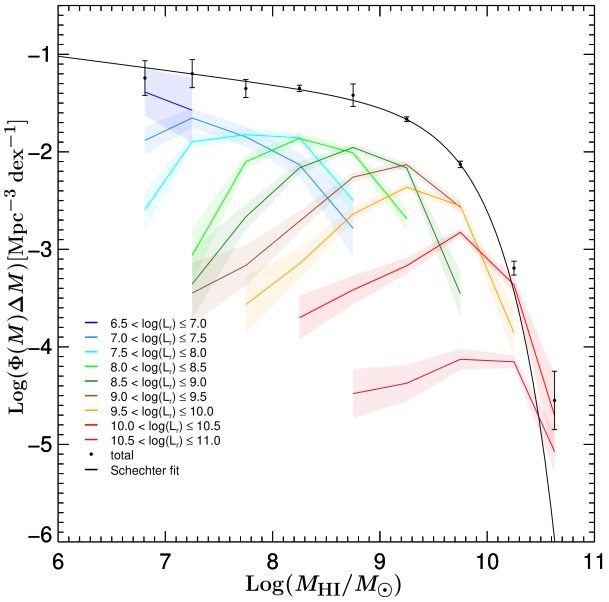

Fig. 7. HI Mass Function (data points and the Schechter function fit to them, in black), and contributions to the HIMF for individual luminosity bins, indicated by different colors (see the legend). Volume densities in each 0.5 dex wide bin in HI mass, log($\Phi(M)\ \Delta M$) in units of Mpc^{-3} dex^{-1}, are shown as a function of HI mass in each luminosity bin. For clarity, we omit data points with volume density values that are smaller than their uncertainties. The black points are the sum of the HI masses in the corresponding luminosity bins. Uncertainties for each luminosity bin are shown as shaded regions around each mass function, with the total quadrature sum shown as error bars on the HIMF. The black line is the Schechter fit to the HIMF.

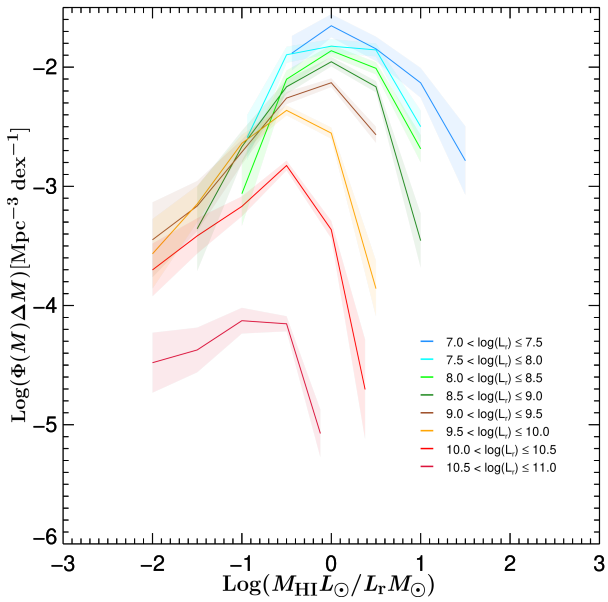

Fig. 8. Volume densities in each 0.5 dex wide bin of HI mass, log($\Phi(M)\Delta M$) in units of Mpc^{-3} dex^{-1}, as a function of gas-to-light ratio, $\log\left(\frac{M_{HI}/M_\odot}{L_r/L_\odot}\right)$ for the same luminosity bins as shown in Fig. 7.

HIMF, based on Nançay data only. Identifying trends as a function of luminosity allowed us to extrapolate the density and gas-to-light distribution values toward the low-luminosity bins with missing galaxies. To analyze the effects of this change in detection fraction with luminosity we constructed two extrapolated BLFs, which we referred to as optically corrected and corrected, respectively. For the optically corrected BLF, we ignored the change in detection fraction as a function of luminosity and set the detection fraction of all log($L_r/L_\odot$) < 7.75 bins equal to that of the lowest luminosity well-sampled 7.75 bin. For the corrected BLF, we included the change in detection fraction with luminosity and set the detection fraction for all log($L_r/L_\odot$) < 9.25 bins equal to that of the 9.25 bin because the fall-off in their detection fractions below this bin are consistent with decreases caused solely by distance and sensitivity effects (see Appendix A in Paper III). Our corrected HIMF agrees well with those derived from the HIPASS and ALFALFA blind surveys Zwaan et al. (2005), Haynes et al. (2011).

Here we expand the analysis to include the Arecibo sample's effect on the optically corrected bivariate distribution. We do not re-examine the corrected distribution, because it attempted to compensate for HI undetected galaxies due to distance and sensitivity effects. Since our Arecibo data are four times more sensitive than the Nançay data, we detect many of the Nançay undetected galaxies that were the reason for the original correction. The decrease in detection rate as a function of color in Figs. 2 and 10 corroborates this claim. Our 100% detection rate for blue galaxies with $g - z < 0.75$ mag is not unexpected. Based on an analysis similar to that in Appendix A of Paper III, we would expect to detect 66 ± 2 of the 69 blue galaxies in our follow-up sample, that is, a detection rate of 96–99%. This estimate is based on our minimum detectable integrated line flux at Arecibo and sampling errors from the standard deviation of the

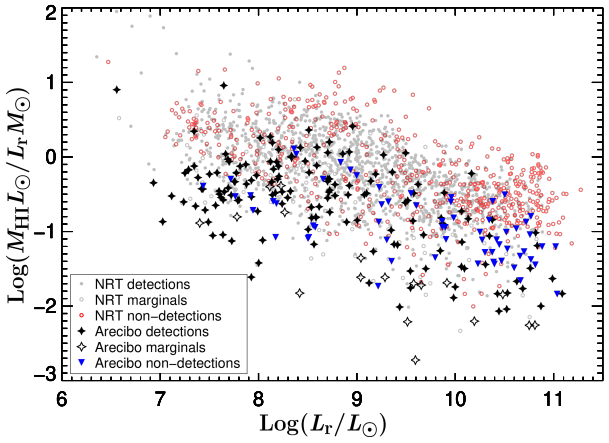

Fig. 9. $\mathrm{Log}\left(\frac{M_{\mathrm{HI}}/M_\odot}{L_r/L_\odot}\right)$, as a function of $\log(L_r/L_\odot)$ for the Arecibo and Nançay samples within the Arecibo sample's declination range. Excluded are sources that were clearly confused or had unreliable photometry. Nançay detections, marginals, and nondetections are represented by gray dots, open gray circles, and open red circles respectively. Arecibo detections, marginals, and nondetections are respectively represented by black solid stars, open stars, and blue downward triangles.

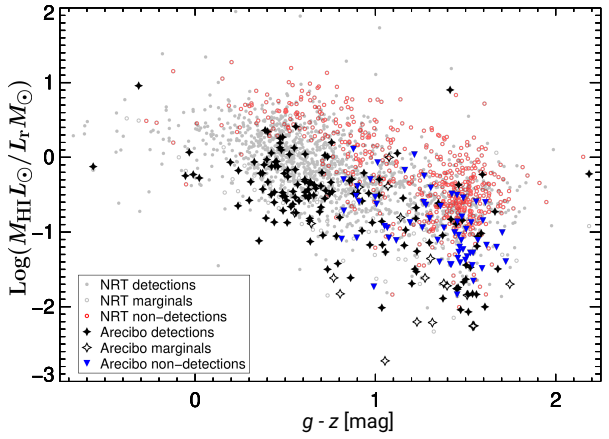

Fig. 10. $\mathrm{Log}\left(\frac{M_{\mathrm{HI}}/M_\odot}{L_r/L_\odot}\right)$ as a function of $g-z$ color for the Arecibo and Nançay samples. Excluded are sources that were clearly confused or had unreliable photometry. Nançay detections, marginals, and nondetections are represented by gray dots, open gray circles, and open red circles respectively. Arecibo detections, marginals, and nondetections are respectively represented by black solid stars, open stars, and blue downward triangles.

binomial distribution, but we do not have a uniform rms noise level due to our observing strategy where initially weak or nondetected sources received follow-up observations.

In contrast to the corrected distribution, the optically corrected distribution only attempts to correct for low-luminosity galaxies that were not included in the original NIBLES sample. In order to extrapolate the bivariate distribution across the full luminosity range (for which the reconstruction of a plausible HIMF was required) we must account for these missing low-luminosity galaxies in our new distribution utilizing the Arecibo follow-up data.

Unlike the Nançay data (see Fig. 8 in Paper III), the Arecibo data do not show any consistent trends with luminosity in the mean, standard deviation and skewness of the gas-to-light ratio over the entire luminosity range. The mean Arecibo gas-to-light ratios, standard deviations and skewness values in luminosity

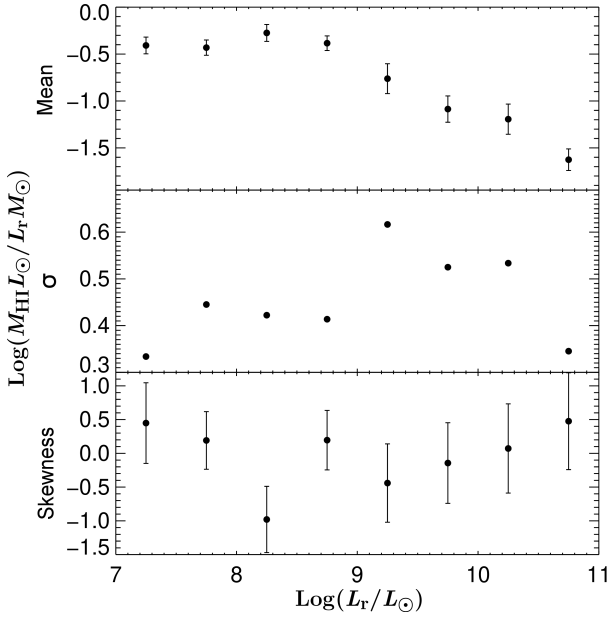

Fig. 11. Properties of the gas-to-light distributions of the Arecibo sample detections as a function of luminosity, in 0.5 dex wide bins of $\log(L_r/L_\odot)$. *Top panel*: mean $\log\left(\frac{M_{\mathrm{HI}}/M_\odot}{L_r/L_\odot}\right)$ ratio, with uncertainties given by the standard error of the mean. *Middle panel*: standard deviation (σ) of the $\log\left(\frac{M_{\mathrm{HI}}/M_\odot}{L_r/L_\odot}\right)$ ratio. *Lowest panel*: skewness of the $\log\left(\frac{M_{\mathrm{HI}}/M_\odot}{L_r/L_\odot}\right)$ ratio.

bins $7.25 \le \log(L_r/L_\odot) \le 8.75$ all agree with one another within the uncertainties, and the gas-to-light ratio distributions can be accurately represented by a nonskewed Gaussian (see Fig. 11).

When correcting the Nançay distributions, we extrapolated gas-to-light ratios for $\log(L_r/L_\odot) \le 7.25$ due to poor detection statistics in those bins. However, for the Arecibo follow-up data, we only extrapolate trends for luminosity bins $\log(L_r/L_\odot) \le 6.75$ due to the $\log(L_r/L_\odot) = 7.25$ bin now having a detection rate of 94% in a sample size of 35.

We first construct extrapolated gas-to-light distributions in low-luminosity bins down to $\log(L_r/L_\odot) = 5.25$ following the same general procedure outlined in Sect. 5.4 of Paper III, but using a nonskewed Gaussian such that within each luminosity bin we have:

$$\Re_j = \int_{\Delta M/2L}^{-\Delta M/2L} \phi \quad \text{and} \quad \mathfrak{F}_k = \int_{\min\ M/L}^{\max\ M/L} \phi \tag{2}$$

where $\Re_j$ is the jth gas-to-light ratio bin, ϕ represents the Gaussian function, and $\mathfrak{F}_k$ is the detection fraction in the kth luminosity bin. $\Delta M/L$ is the $\log\left(\frac{M_{\mathrm{HI}}/M_\odot}{L_r/L_\odot}\right)$ bin size.

We then combine the resulting distribution with the Nançay-based distribution using the same procedure described in Sect. 4.

The resulting reconstructed HIMF is shown in Fig. 12. As with the combined Nançay/Arecibo distribution shown in Fig. 7, we also omit the points on the extremities of the luminosity bins due to their large uncertainties and for viewing clarity. We present the values with their associated fractional uncertainties for luminosity bins $\log(L_r/L_\odot) \le 8.25$ in Table 2. The HI mass distributions for the $\log(L_r/L_\odot) \le 7.75$ bins are more flattened than the corresponding bins in Fig. 9 from Paper III, showing a density increase of ∼0.5−1 dex for the lowest HI mass bins within each luminosity bin; due to the increased density of low $\log\left(\frac{M_{\mathrm{HI}}/M_\odot}{L_r/L_\odot}\right)$ ratio distributions. The Schechter fit parameters for

Table 2. *r*-band luminosity–HI mass distribution function for the corrected combined Nançay and Arecibo distribution.

	Log($L_r/L_\odot$)						
$\log\left(\frac{M_{HI}}{M_\odot}\right)$	5.25	5.75	6.25	6.75	7.25	7.75	8.25
	[volume density in Mpc^{-3} dex^{-1}]						
9.75							−5.31 ± 2.28
9.25						−3.62 ± 0.43	−2.68 ± 0.11
8.75					−3.08 ± 0.35	−2.50 ± 0.11	−2.01 ± 0.04
8.25			−3.35 ± 0.51	−2.44 ± 0.20	−2.00 ± 0.04	−1.86 ± 0.05	−1.86 ± 0.06
7.75	−3.70 ± 0.69	−2.57 ± 0.31	−1.95 ± 0.08	−1.73 ± 0.03	−1.76 ± 0.04	−1.82 ± 0.07	−2.10 ± 0.10
7.25	−1.97 ± 0.16	−1.59 ± 0.03	−1.57 ± 0.04	−1.74 ± 0.06	−1.73 ± 0.13	−1.90 ± 0.10	−3.07 ± 0.17
6.75	−1.36 ± 0.04	−1.49 ± 0.05	−1.75 ± 0.10	−1.71 ± 0.25	−1.91 ± 0.18	−2.59 ± 0.16	−3.43 ± 0.22
6.25	−1.48 ± 0.07	−1.78 ± 0.17	−1.62 ± 0.29	−1.70 ± 0.31	−2.84 ± 0.34	−2.97 ± 0.19	−4.08 ± 0.26
5.75	−1.82 ± 0.26	−1.52 ± 0.31	−1.56 ± 0.31	−2.34 ± 0.27			
5.25	−1.40 ± 0.32	−1.42 ± 0.30	−2.20 ± 0.27	−3.75 ± 0.25			

Notes. Volume densities are $\log(\Phi(M_{HI},L_r)\Delta M\ \Delta L)$ in Mpc^{-3} dex^{-1}. The listed uncertainties are fractional.

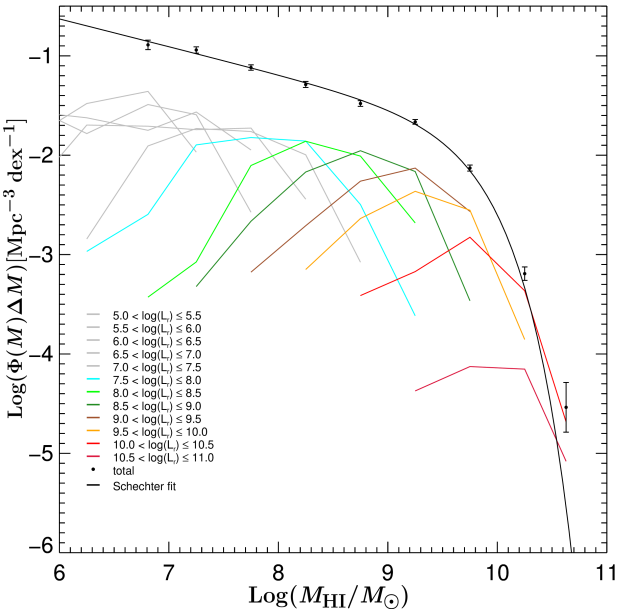

Fig. 12. Reconstructed HI Mass Function based on the combined optically corrected Nançay and Arecibo distributions (data points and the Schechter function fit to them, in black), and contributions to the HIMF for individual luminosity bins, indicated by different colors (see the Legend). Volume densities are shown in each 0.5 dex wide bin in HI mass, $\log(\Phi(M)\Delta M)$, in units of Mpc^{-3} dex^{-1}. We recreated a plot similar to Fig. 7 with artificial, extrapolated HI mass distributions for luminosity bins below $\log(L_r/L_\odot) = 7.75$ shown in gray. For viewing clarity we omit points with uncertainties larger than the density values and do not show the uncertainty regions on each luminosity bin. Uncertainties for the corrected bins are given in Table 2.

the reconstructed HIMF are:

$\Phi = 0.009 \pm 0.002$, $\log(M_\star/M_\odot) = 9.70 \pm 0.06$, $\alpha = -1.28 \pm 0.03$.

This result agrees very well with the optically corrected HIMF from Paper III:

$\Phi = 0.0085 \pm 0.0015$, $\log(M_\star/M_\odot) = 9.72 \pm 0.06$, $\alpha = -1.26 \pm 0.04$

and with the HIMF from Zwaan et al. (2003):

$\Phi = 0.0086$, $\log(M_\star/M_\odot) = 9.79$, $\alpha = -1.30$.

While our "corrected" distribution (accounting for drop-offs in detection statistics due to distance and sensitivity effects at Nançay) from Paper III produced an HIMF that agreed well with the HIMF from Zwaan et al. (2005), our corrected distribution presented here (using Arecibo data in lieu of the sensitivity correction) agrees better with the Zwaan et al. (2003) results, showing that our increased detection statistics in the low luminosity bins did not drastically alter the low mass slope of the HIMF in comparison with the "optically corrected" distribution from Paper III.

The similarity between the reconstructed HIMFs both with and without the Arecibo data illustrates the point that the HIMF is defined by the relatively higher gas-to-light ratio sources within each luminosity bin. Therefore, the details of the gas-to-light distributions as a function of optical luminosity are lost when examining only a single dimension such as the LF or HIMF. The only way to fully quantify the volume density of galaxies in terms of both HI mass and optical luminosity, is to use a two-dimensional distribution. This point should be of particular interest to galaxy evolution modelers as it illustrates a missing dimension in attempts to fit models to observed distributions. For example, a multitude of semi-analytic model studies have been conducted (see, e.g., White & Frenk 1991; Katz et al. 1992; Kauffmann et al. 1993; Cole et al. 1994, 2000; Somerville & Primack 1999; Pearce et al. 2001; Benson et al. 2003; Cooray & Milosavljević 2005) that use either a one-dimensional LF or HIMF as a basis for comparisons with observations. Comparing models with a two-dimensional distribution could help fine-tune various aspects of evolutionary models that is not possible when examining only a single dimension.

6. Conclusions

We presented data from the third and final Arecibo HI follow-up campaign of Nançay nondetections of NIBLES galaxies, combining this data with our previous two Arecibo campaigns to create a random subsample spanning the range in luminosity and $g - i$ color of the NIBLES sample. We used this follow-up data to create a two dimensional bivariate luminosity–HI mass

distribution that we then scaled by the HI undetected fractions of the Nançay uncorrected and optically corrected distributions.

Combining the resulting scaled Arecibo distribution with our original Nançay distributions resulted in a net density increase of about 10% at the low gas-to-light ratio bins ($-1.0 < \log\left(\frac{M_{\rm HI}/M_\odot}{L_r/L_\odot}\right) < -0.5$) within each luminosity bin. The effect on the uncorrected bivariate distribution resulted in a HIMF with a steeper low mass slope, but one that is just shallow of recent blind survey HIMFs (with the slope disagreeing just outside the uncertainty range).

However, the bins with the lowest luminosities for the optically corrected BLF saw density increases of ~0.5 to 1 dex for the highest gas-to-light ratio bins while producing a minimal change to the resulting HIMF low mass slope. This result illustrates the point that there may be significant deviations in the volume density for galaxies on the outskirts of the gas-to-light ratio distributions, as a function of environment or other factors, which we are currently unable to probe with a one-dimensional distribution.

Our results confirm that low gas-to-light ratio galaxies contribute relatively little to the overall HI volume density of the universe and that optically selected samples tend to lack adequate numbers of high gas-to-light ratio galaxies from which to construct a realistic HIMF. However, the low gas-to-light ratio galaxies provide valuable insight into the gas-to-light distributions of the overall galaxy population and will aid our understanding of evolutionary processes within these galaxies.

Acknowledgements. The Arecibo Observatory is a facility of the National Science Foundation operated under cooperative agreement (AST-1744119) by the University of Central Florida in alliance with Universidad Ana G. Méndez (UAGM) and Yang Enterprises (YEI), Inc. The Nançay Radio Telescope is operated as part of the Paris Observatory, in association with the Centre National de la Recherche Scientifique (CNRS) and partially supported by the Région Centre in France. Funding for SDSS-III has been provided by the Alfred P. Sloan Foundation, the Participating Institutions, the National Science Foundation, and the US Department of Energy Office of Science. The SDSS-III website is http://www.sdss3.org/. SDSS-III is managed by the Astrophysical Research Consortium for the Participating Institutions of the SDSS-III Collaboration including the University of Arizona, the Brazilian Participation Group, Brookhaven National Laboratory, Carnegie Mellon University, University of Florida, the French Participation Group, the German Participation Group, Harvard University, the Instituto de Astrofisica de Canarias, the Michigan State/Notre Dame/JINA Participation Group, Johns Hopkins University, Lawrence Berkeley National Laboratory, Max Planck Institute for Astrophysics, Max Planck Institute for Extraterrestrial Physics, New Mexico State University, New York University, Ohio State University, Pennsylvania State University, University of Portsmouth, Princeton University, the Spanish Participation Group, University of Tokyo, University of Utah, Vanderbilt University, University of Virginia, University of Washington, and Yale University. We would like to thank the anonymous referee for their helpful comments and constructive feedback to improve this article.

References

Benson, A. J., Bower, R. G., Frenk, C. S., et al. 2003, ApJ, 599, 38
Blanton, M. R., Hogg, D. W., Brinkmann, J., et al. 2003, ApJ, 592, 819
Butcher, Z., Schneider, S., van Driel, W., Lehnert, M. D., & Minchin, R. 2016, A&A, 596, A60
Butcher, Z., Schneider, S., van Driel, W., & Lehnert, M. D. 2018, A&A, 619, A89
Cole, S., Aragon-Salamanca, A., Frenk, C. S., Navarro, J. F., & Zepf, S. E. 1994, MNRAS, 271, 781
Cole, S., Lacey, C. G., Baugh, C. M., & Frenk, C. S. 2000, MNRAS, 319, 168
Cooray, A., & Milosavljević, M. 2005, ApJ, 627, L89
Geller, M. J., Diaferio, A., Kurtz, M. J., Dell'Antonio, I. P., & Fabricant, D. G. 2012, AJ, 143, 102
Haynes, M. P., Giovanelli, R., Martin, A. M., et al. 2011, AJ, 142, 170 (H11)
Hoppmann, L., Staveley-Smith, L., Freudling, W., et al. 2015, MNRAS, 452, 3726
Katz, N., Hernquist, L., & Weinberg, D. H. 1992, ApJ, 399, L109
Kauffmann, G., White, S. D. M., & Guiderdoni, B. 1993, MNRAS, 264, 201
Kovac, K., Oosterloo, T. A., & van der Hulst, J. M. 2005, in IAU Colloq. 198: Near-fields Cosmology with Dwarf Elliptical Galaxies, ed. H. Jerjen, 351
Lan, T.-W., Ménard, B., & Mo, H. 2016, MNRAS, 459, 3998
Lemonias, J. J., Schiminovich, D., Catinella, B., Heckman, T. M., & Moran, S. M. 2013, ApJ, 776, 74
Loveday, J. 2002, Cont. Phys., 43, 437
Loveday, J., Peterson, B. A., Efstathiou, G., & Maddox, S. J. 1992, ApJ, 390, 338
Loveday, J., Norberg, P., Baldry, I. K., et al. 2015, MNRAS, 451, 1540
Martin, A. M., Papastergis, E., Giovanelli, R., et al. 2010, ApJ, 723, 1359
Marzke, R. O., Geller, M. J., Huchra, J. P., & Corwin, H. G., Jr. 1994, AJ, 108, 437
McNaught-Roberts, T., Norberg, P., Baugh, C., et al. 2014, MNRAS, 445, 2125
Montero-Dorta, A. D., & Prada, F. 2009, MNRAS, 399, 1106 (M09)
Norberg, P., Cole, S., Baugh, C. M., et al. 2002, MNRAS, 336, 907
Parsa, S., Dunlop, J. S., McLure, R. J., & Mortlock, A. 2016, MNRAS, 456, 3194
Pearce, F. R., Jenkins, A., Frenk, C. S., et al. 2001, MNRAS, 326, 649
Rao, S., & Briggs, F. 1993, ApJ, 419, 515
Saintonge, A. 2007, AJ, 133, 2087
Schechter, P. 1976, ApJ, 203, 297
Schlegel, D. J., Finkbeiner, D. P., & Davis, M. 1998, ApJ, 500, 525
Schneider, S. E., Helou, G., Salpeter, E. E., & Terzian, Y. 1986, AJ, 92, 742
Schneider, S. E., Thuan, T. X., Magri, C., & Wadiak, J. E. 1990, ApJS, 72, 245
Schneider, S. E., Spitzak, J. G., & Rosenberg, J. L. 1998, ApJ, 507, L9
Somerville, R. S., & Primack, J. R. 1999, MNRAS, 310, 1087
Springob, C. M., Haynes, M. P., Giovanelli, R., & Kent, B. R. 2005, ApJS, 160, 149
van Driel, W., Butcher, Z., Schneider, S., et al. 2016, A&A, 595, A118
White, S. D. M., & Frenk, C. S. 1991, ApJ, 379, 52
York, D. G., Adelman, J., Anderson, J. E., Jr., et al. 2000, AJ, 120, 1579
Zwaan, M. A., Briggs, F. H., Sprayberry, D., & Sorar, E. 1997, ApJ, 490, 173
Zwaan, M. A., Staveley-Smith, L., Koribalski, B. S., et al. 2003, AJ, 125, 2842 (Z03)
Zwaan, M. A., Meyer, M. J., Staveley-Smith, L., & Webster, R. L. 2005, MNRAS, 359, L30

Appendix A: Arecibo HI line data

Color SDSS images along with Arecibo HI line spectra of all 151 galaxies from the final follow-up HI observing campaign are shown in Fig. A.1 for Arecibo detections, in Fig. A.2 for marginal detections, and in Fig. A.3 for nondetections. Selected properties of the three categories of galaxy detections are listed in Tables A.1–A.3 respectively.

Listed throughout the tables are the following properties of the target galaxies:

- source: NIBLES sample source number (see Paper I);
- RA and Dec: Right Ascension and Declination in J2000.0 coordinates, as used for the observations;
- Name: common catalog name, other than the SDSS;
- $V_{\rm opt}$: heliocentric recession velocity from the SDSS redshift, determined in the optical convention (in km s^{-1}), from Paper II;
- $g-z$: $g-z$ extinction-corrected (following Schlegel et al. 1998) color of the galaxy using SDSS model magnitudes;
- $M_{\rm g}$: extinction corrected absolute g-band magnitude;
- $\log(M_\star/M_\odot)$: total median stellar mass estimates;
- $\log(L_r/L_\odot)$: SDSS r-band luminosity derived from Petrosian magnitudes as in Paper III;
- $\log({\rm sSFR/yr}^{-1})$: specific Star Formation Rate, or SFR/$M_\star$;
- rms: rms noise level values of the HI spectra (in mJy);
- $V_{\rm HI}$: heliocentric recession velocity of the center of the HI line profile (in km s^{-1});
- W_{50}, W_{20}: velocity widths measured at 50% and 20% of the HI profile peak level, respectively, uncorrected for galaxy inclination (in km s^{-1});
- $F_{\rm HI}$: integrated HI line flux (in Jy km s^{-1});
- SNR: peak signal-to-noise ratio, which we define as the peak flux density divided by the rms. For nondetections, the SNR listed is the maximum found in the expected velocity range of the HI profile;
- S/N: signal-to-noise, determined taking into account the line width, following the ALFALFA HI survey formulation from Saintonge (2007): $S/N = 1000(F_{\rm HI}/W_{50})\cdot(W_{50}/2\cdot R)^{0.5}/{\rm rms}$, where R is the velocity resolution, 18.7 km s^{-1};
- $\log(M_{\rm HI}/M_\odot)$: Total HI mass, where $M_{\rm HI} = 2.36\times10^5\cdot D^2\cdot F_{\rm HI}$, where $D = V/70$ is the galaxy's distance (in Mpc). In the cases of nondetections, 3σ upper limits are listed for a flat-topped profile with a width depending on the target's r-band luminosity, L_r, according to the upper envelope in the W_{20} – $\log(L_r/L_\odot)$ relationship of our Nançay clear, nonconfused detections (see Paper I) – these are quite conservative upper limits;
- $\log(M_{\rm HI}/M_\star)$: ratio of the total HI and stellar masses (in $M_\odot$).

Estimated uncertainties are given after the values in the tables. Uncertainties in the central HI line velocity, $V_{\rm HI}$, and in the integrated HI line flux, $F_{\rm HI}$, were determined following Schneider et al. (1986, 1990) as, respectively

$$\sigma_{v_{\rm HI}} = 1.5(W_{20}-W_{50}){\rm SNR}^{-1}\ ({\rm km\,s^{-1}}) \quad (A.1)$$

and

$$\sigma_{F_{\rm HI}} = 2(1.2W_{20}R)^{0.5}{\rm rms}\ ({\rm Jy\,km\,s^{-1}}) \quad (A.2)$$

where R is the instrumental resolution, 18.7 km s^{-1}, SNR is the peak signal-to-noise ratio of a spectrum and rms is the rms noise level (in Jy). Following Schneider et al., the uncertainty in the W_{50} and W_{20} line widths is expected to be 2 and 3.1 times the uncertainty in $V_{\rm HI}$, respectively.

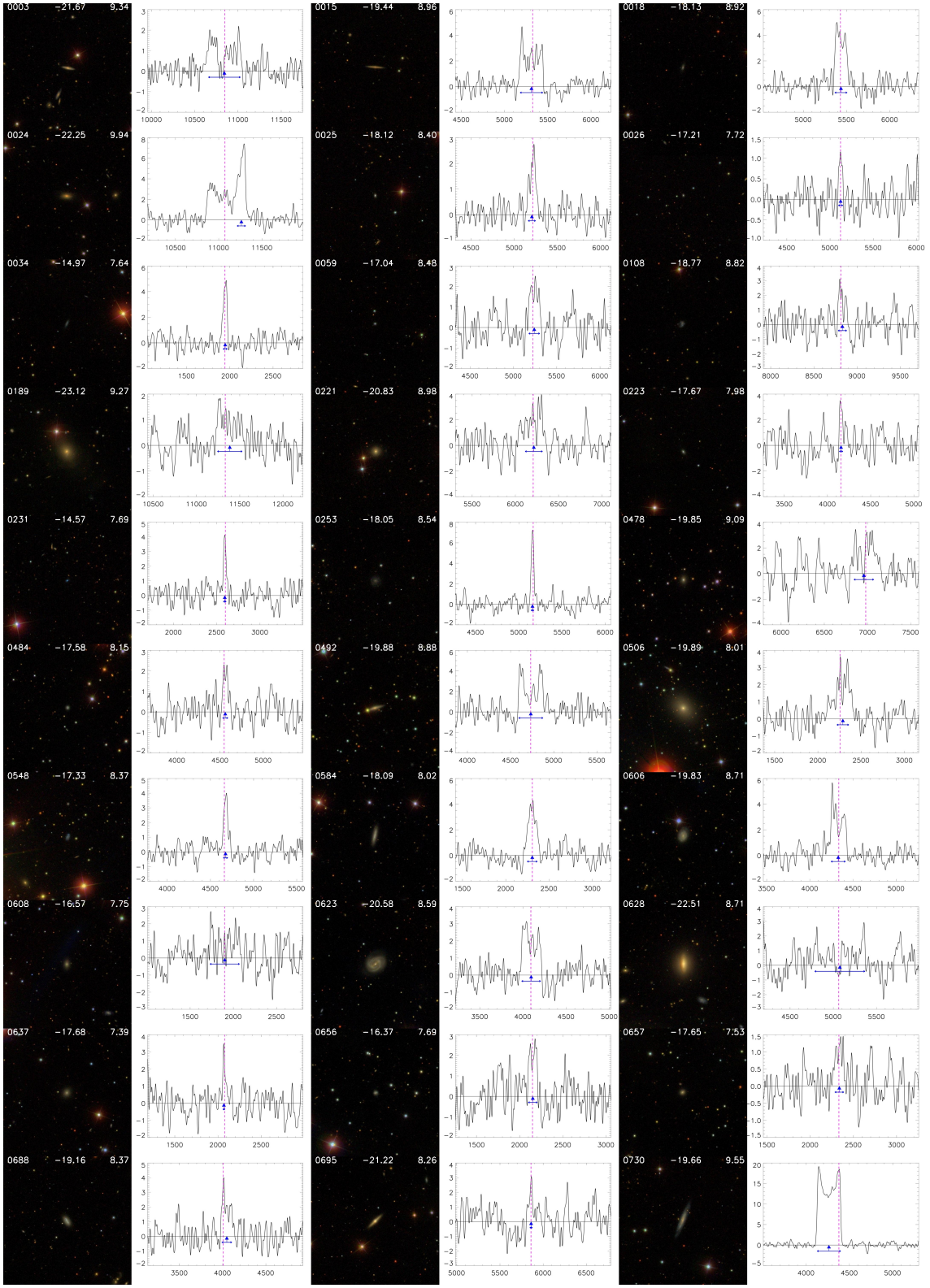

Fig. A.1. Color (g, r and i band composite) images from the SDSS alongside 21 cm HI line spectra of galaxies clearly detected at Arecibo. The size of each image is $2' \times 2'$ with the NIBLES source number indicated in the upper left corner, absolute z-band magnitude, M_z, in the top center and $\log(M_{\rm HI}/M_\odot)$ in the top right corner of each image. The vertical axis in the spectra is flux density in mJy, the horizontal axis is heliocentric recession velocity (cz) in km s^{-1}. The SDSS recession velocity is denoted by a vertical dashed magenta line, the mean HI velocity by the blue triangle, and the W_{50} line width by the horizontal blue arrow bar. Velocity resolution is 18.7 km s^{-1}. Confused galaxies are denoted by a C in the upper right portion of the spectrum. See Paper II for codes used in the previous campaigns.

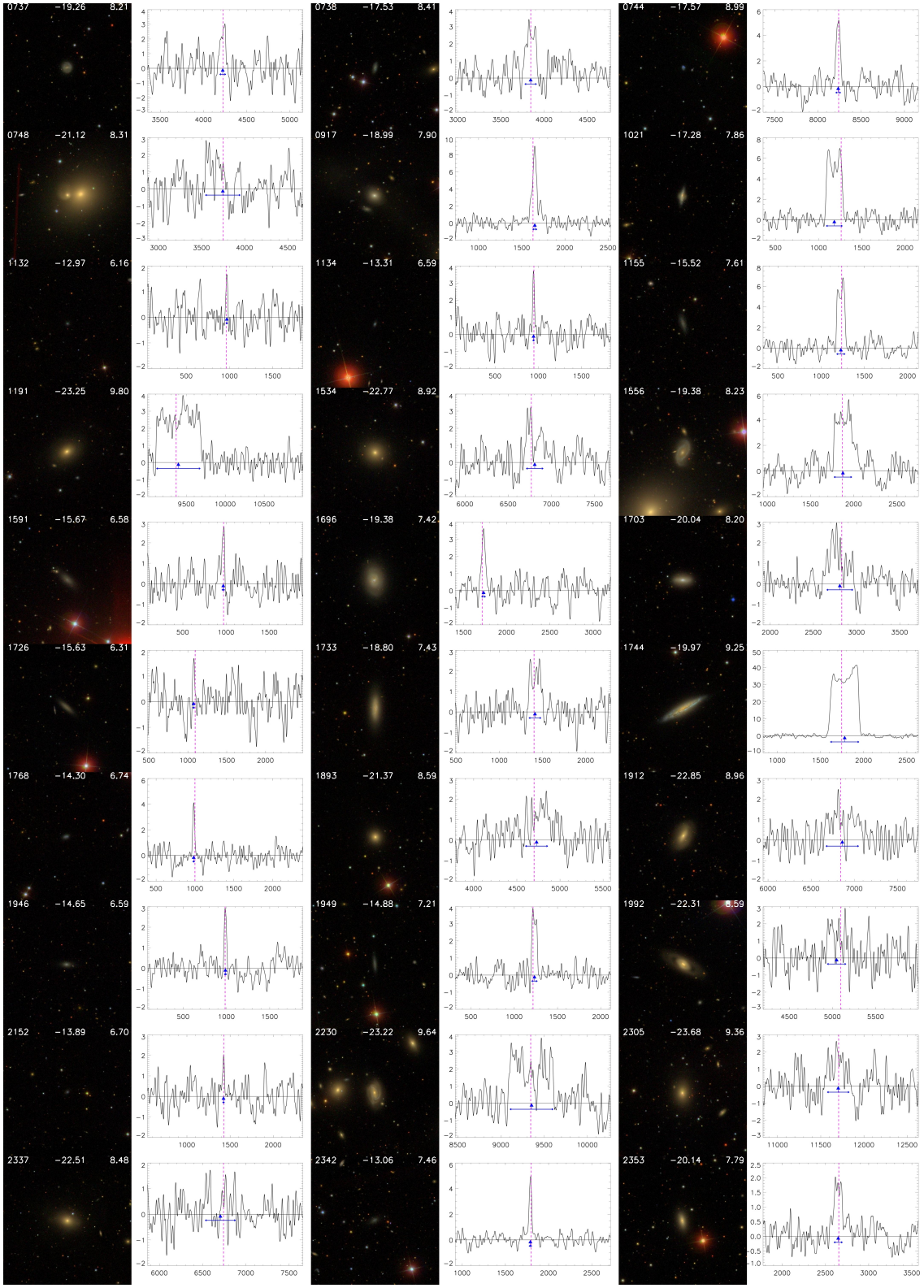

Fig. A.1. continued.

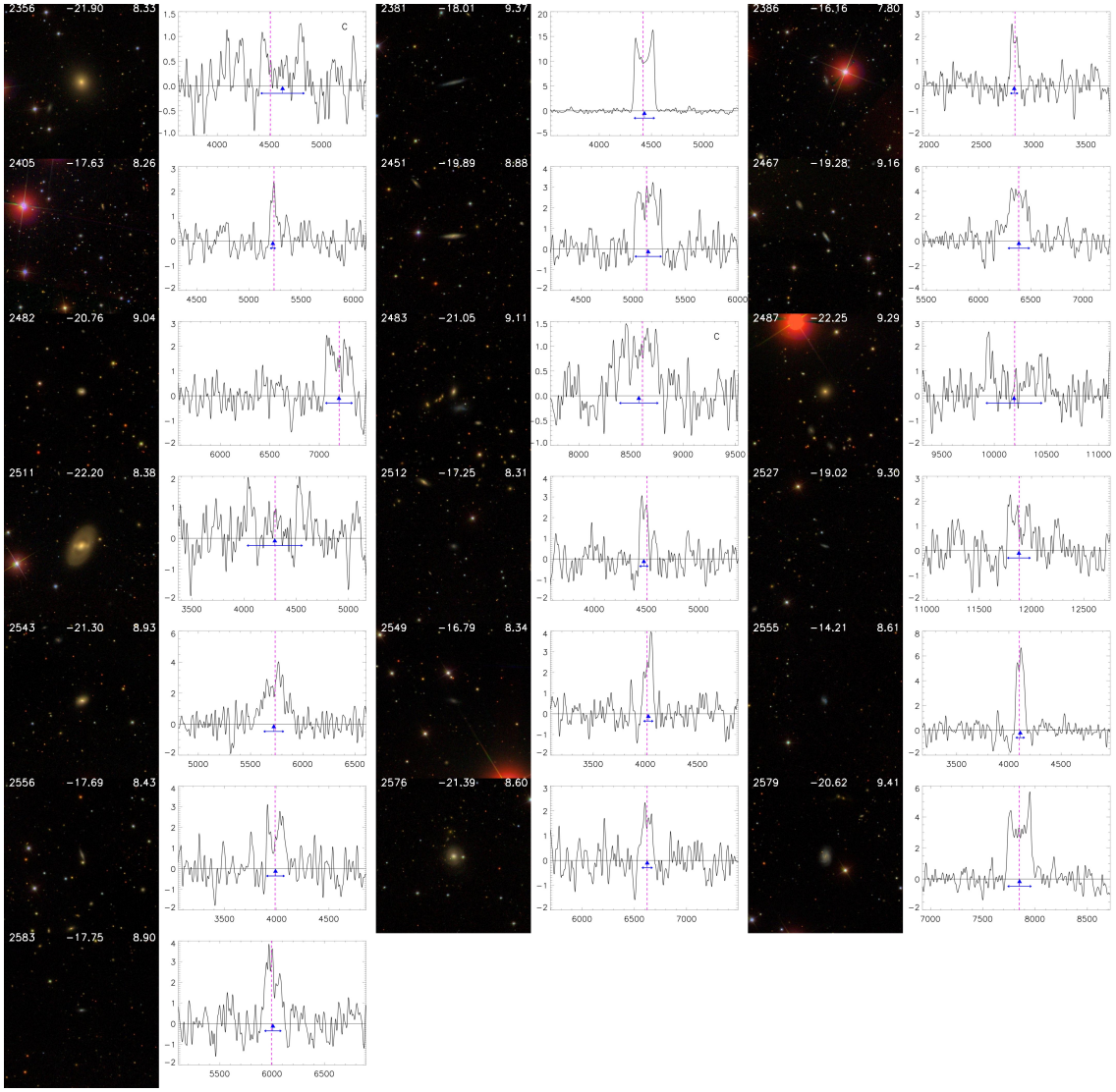

Fig. A.1. continued.

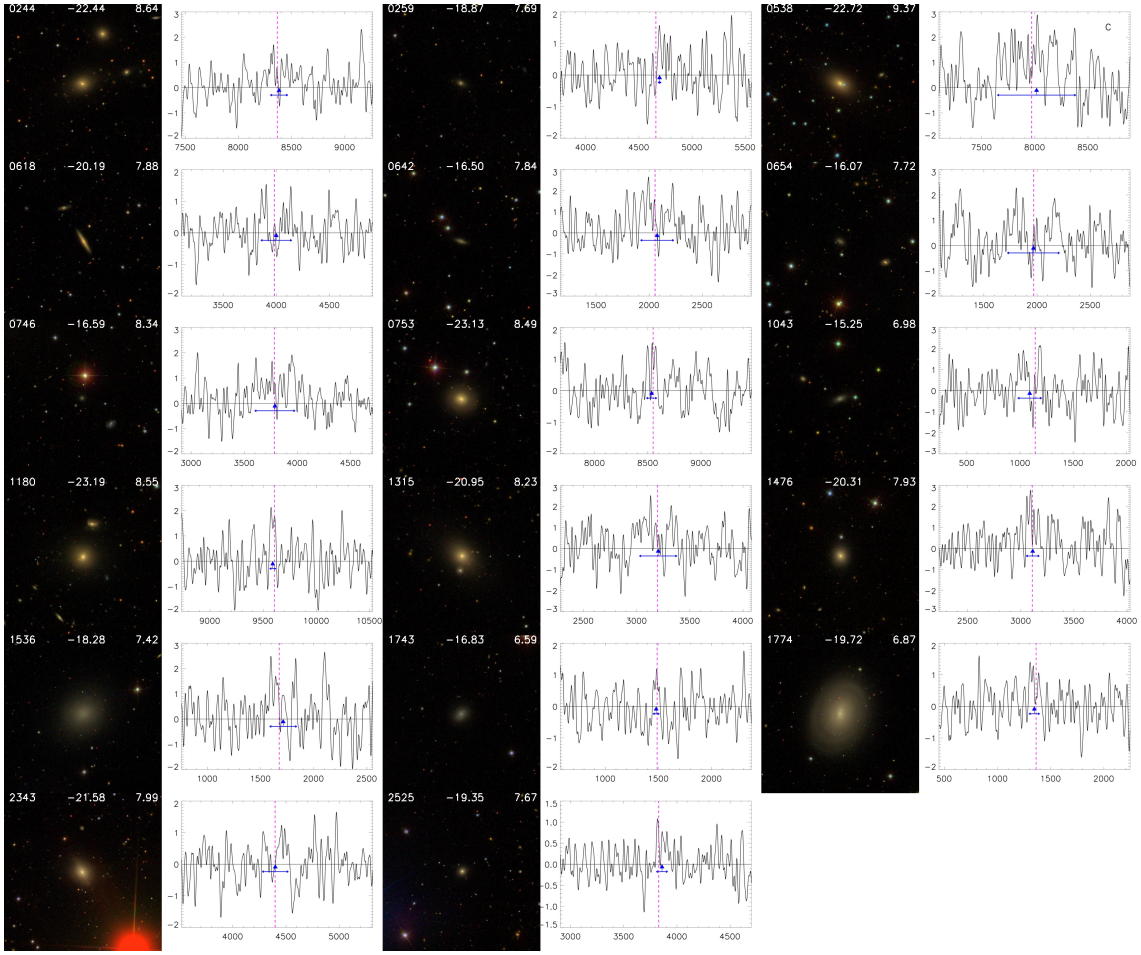

Fig. A.2. Color images from the SDSS alongside the 21-cm Hi line spectra of galaxies marginally detected at Arecibo. See Fig. A.1 for further details.

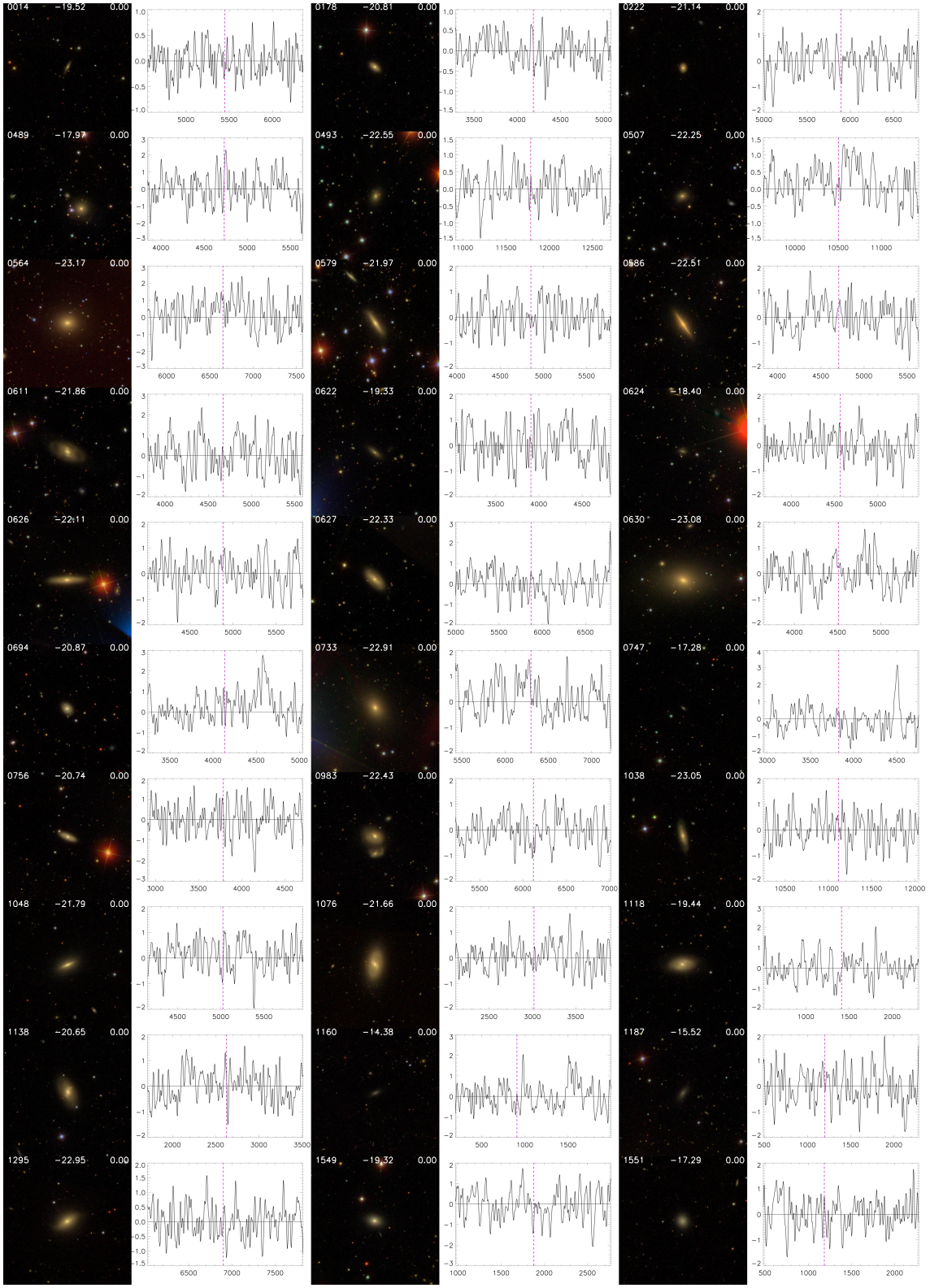

Fig. A.3. Color images from the SDSS alongside the 21-cm Hi line spectra of galaxies undetected at Arecibo. See Fig. A.1 for further details.

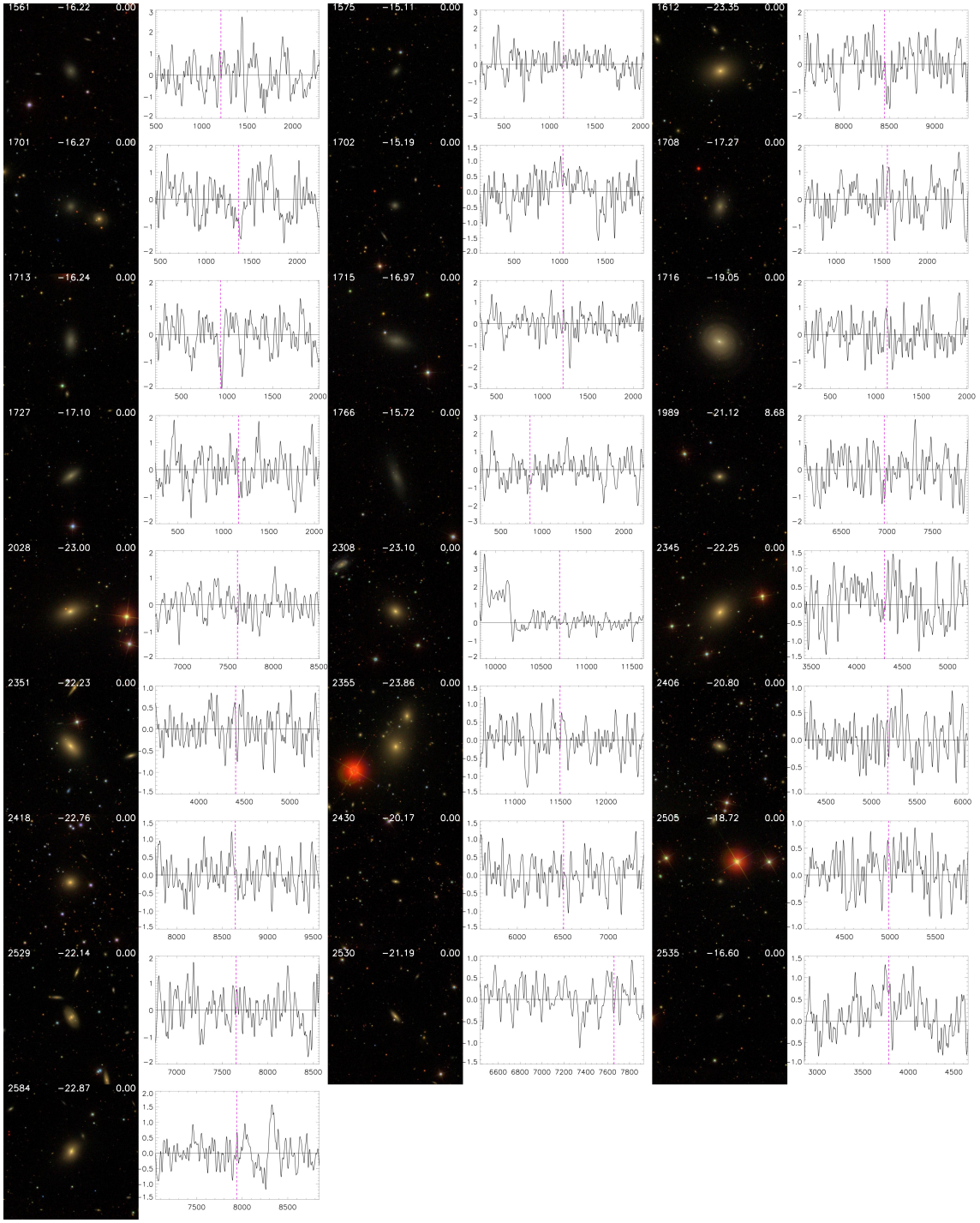

Fig. A.3. continued.

Table A.3. Basic optical and HI data – Arecibo nondetections of Nançay nondetections and marginals.

Source	RA	Dec	Name	V_{opt}	$g-z$	M_g	$\log(M_\star)$	$\log\left(\frac{L_r}{L_\odot}\right)$	$\log\left(\frac{sSFR}{yr^{-1}}\right)$	rms	$\log\left(\frac{M_{HI}}{M_\odot}\right)$	$\log\left(\frac{M_{HI}}{M_\star}\right)$
	(J2000.0)											
				(km s^{-1})	(mag)	(mag)				(mJy)		
0014	00 06 19.61	14 19 38.70	2MASX J00061957+1419389	5448 ± 3	1.31	−18.22	9.66	9.23	−11.16	0.43	<7.54	<−2.11
0178	01 15 54.30	13 21 12.00	CGCG 436−016	4184 ± 2	1.46	−19.35	10.24	9.87	−12.12	0.81	<7.58	<−2.66
0222	01 31 04.80	13 38 58.80	CGCG 436−067	5889 ± 2	1.61	−19.53	10.49	9.96	−12.29	0.87	<7.92	<−2.57
0489	07 37 49.90	28 39 10.50	2MASX J07374992+2839102	4731 ± 7	1.01	−16.96	8.86	8.84	−11.18	0.60	<7.55	<−1.31
0493	07 38 32.50	29 11 07.90	CGCG 147−048	11784 ± 4	1.45	−21.09	10.91	10.50	−12.24	0.74	<8.46	<−2.45
0507	07 40 27.50	30 48 20.00	2MASX J07402743+3048201	10503 ± 2	1.56	−20.69	10.87	10.38	−12.26	0.61	<8.26	<−2.61
0564	07 59 29.70	27 01 35.10	NGC 2492	6649 ± 2	1.50	−21.67	11.23	10.77	−12.48	0.51	<7.79	<−3.44
0579	08 02 57.50	16 17 57.50	UGC 04190	4853 ± 2	1.53	−20.44	10.77	10.30	−12.62	0.51	<7.52	<−3.25
0586	08 06 13.40	17 42 23.60	NGC 2522	4706 ± 2	1.72	−20.78	11.05	10.47	−12.37	0.56	<7.54	<−3.50
0611	08 17 35.00	20 54 11.00	NGC 2553	4670 ± 1	1.48	−20.38	10.64	10.27	−12.35	0.77	<7.66	<−2.98
0622	08 19 24.28	21 00 12.80	2MASX J08192430+2100125	3906 ± 4	1.28	−18.05	9.67	9.25	−12.38	0.51	<7.32	<−2.35
0624	08 19 36.04	21 14 28.90	2MASX J08193606+2114291	4566 ± 8	1.27	−17.13	9.17	9.00	−11.62	0.58	<7.50	<−1.66
0626	08 19 51.90	20 59 05.90	NGC 2560	4883 ± 2	1.54	−20.57	10.78	10.38	−12.04	0.58	<7.56	<−3.22
0627	08 20 09.90	27 05 36.50	UGC 04341	5869 ± 2	1.62	−20.72	10.92	10.45	−11.46	0.58	<7.73	<−3.19
0630	08 20 35.70	21 04 04.00	NGC 2563	4509 ± 2	1.54	−21.55	11.10	10.81	−12.52	1.02	<7.75	<−3.35
0694	08 38 09.63	19 43 32.40	NGC 2624	4134 ± 1	1.38	−19.49	10.21	9.90	−10.62	0.73	<7.54	<−2.67
0733	08 46 49.20	28 10 16.70	IC 2393	6297 ± 2	1.51	−21.41	11.09	10.66	−12.35	0.52	<7.68	<−3.42
0747	08 49 15.01	19 11 27.30	PGC 4572078	3827 ± 11	1.22	−16.06	8.71	8.38	−11.30	0.52	<7.32	<−1.39
0756	08 54 40.70	20 35 00.90	CGCG 120−050	3785 ± 1	1.35	−19.39	10.15	9.91	−11.81	0.61	<7.38	<−2.78
0983	10 03 58.80	22 16 33.80	UGC 05420	6120 ± 2	1.49	−20.94	10.93	10.53	−12.64	0.54	<7.70	<−3.23
1038	10 21 21.10	24 20 29.00	UGC 05591	11118 ± 2	1.53	−21.52	11.21	10.72	−11.99	0.53	<8.25	<−2.96
1048	10 25 47.70	26 34 14.60	CGCG 154−013	5023 ± 2	1.44	−20.35	10.62	10.25	−12.04	0.81	<7.69	<−2.92
1076	10 36 38.40	14 10 15.90	NGC 3300	3017 ± 1	1.42	−20.24	10.53	10.23	−12.29	0.81	<7.31	<−3.23
1118	10 50 45.50	28 28 08.70	NGC 3400	1412 ± 1	1.36	−18.09	–	9.35	–	0.81	<6.65	–
1138	10 58 37.60	09 03 01.60	UGC 06062	2623 ± 2	1.46	−19.20	10.18	9.80	−12.22	0.59	<7.05	<−3.14
1160	11 04 56.80	17 38 30.50	PGC 4263693	907 ± 6	0.90	−13.48	7.39	7.44	−10.61	0.62	<6.08	<−1.31
1187	11 12 31.70	16 17 22.60	LSBC F640−V04	1198 ± 15	0.89	−14.63	–	7.92	–	0.63	<6.40	–
1295	11 31 42.00	28 09 12.90	NGC 3713	6898 ± 2	1.46	−21.49	11.07	10.70	−12.06	0.53	<7.79	<−3.29
1549	12 11 02.70	12 06 14.40	IC 0767	1877 ± 2	1.12	−18.21	9.41	9.30	−10.70	0.81	<6.87	<−2.55
1551	12 11 07.80	14 16 29.30	IC 3032	1184 ± 5	1.05	−16.24	–	8.56	–	0.81	<6.49	–
1561	12 12 18.90	15 28 59.10	VCC 0050	1209 ± 12	0.91	−15.31	–	8.15	–	0.79	<6.51	–
1575	12 15 08.50	14 58 18.70	VCC 0137	1152 ± 7	0.97	−14.14	–	7.72	–	0.79	<6.40	–
1612	12 19 47.60	30 20 20.70	NGC 4272	8446 ± 2	1.47	−21.89	11.26	10.88	−12.42	0.58	<8.06	<−3.20
1701	12 39 37.70	10 58 32.60	VCC 1803	1355 ± 21	1.01	−15.27	8.24	8.18	−11.23	0.62	<6.48	<−1.75
1702	12 39 42.80	13 36 26.80	VCC 1806	1034 ± 8	1.00	−14.19	–	7.76	–	0.62	<6.24	–
1708	12 40 13.40	12 52 29.10	IC 3635	1560 ± 8	1.07	−16.20	8.69	8.58	−11.76	0.46	<6.44	<−2.25
1713	12 41 39.40	12 14 50.60	IC 3663	927 ± 10	0.90	−15.34	–	8.17	–	0.46	<6.02	–
1715	12 41 46.10	11 29 19.10	IC 3665	1227 ± 29	0.81	−16.16	–	8.50	–	0.46	<6.26	–
1716	12 41 59.40	12 56 34.20	NGC 4620	1125 ± 3	0.99	−18.06	–	9.22	–	0.46	<6.16	–
1727	12 47 20.60	12 09 59.10	IC 3779	1165 ± 4	1.07	−16.03	–	8.51	–	0.54	<6.27	–
1766	12 58 09.00	14 51 32.10	UGC 08081	853 ± 16	0.83	−14.90	–	7.94	–	0.83	<6.17	–
1989	13 57 29.52	09 57 03.20	CGCG 074−017	6969 ± 2	1.30	−19.82	10.29	9.98	−11.92	0.40	<7.73	<−2.56
2028	14 04 45.70	14 22 55.30	NGC 5454	7603 ± 1	1.46	−21.54	11.03	10.76	−12.22	0.83	<8.12	<−2.91
2308	15 23 35.20	09 20 46.10	CGCG 077−110	10703 ± 2	1.48	−21.62	11.22	10.77	−12.38	0.75	<8.33	<−2.89
2345	15 57 08.10	22 24 16.40	NGC 6020	4304 ± 2	1.42	−20.83	10.84	10.40	−12.83	0.54	<7.43	<−3.40
2351	16 01 51.40	17 57 26.90	NGC 6030	4403 ± 1	1.47	−20.76	10.74	10.39	−12.03	0.54	<7.41	<−3.34
2355	16 02 19.80	16 20 45.70	UGC 10144	11494 ± 3	1.67	−22.19	11.53	11.02	−12.58	0.40	<8.16	<−3.37
2406	21 16 24.80	10 16 24.10	CGCG 426−029	5175 ± 2	1.26	−19.54	10.15	9.87	−11.09	0.45	<7.50	<−2.65
2418^M	21 31 37.60	11 49 53.90	CGCG 426−062	8643 ± 3	1.70	−21.05	11.15	10.52	−12.19	0.45	<7.91	<−3.23
2430	21 50 27.60	12 38 10.30	2MASX J21502753+1238103	6507 ± 2	1.42	−18.75	9.98	9.55	−11.69	0.45	<7.67	<−2.30
2505	23 12 22.70	14 30 22.60	2MASX J23122267+1430223	4982 ± 6	1.16	−17.55	9.24	8.93	−11.11	0.51	<7.54	<−1.70
2529	23 23 27.00	14 19 33.00	CGCG 431−053	7651 ± 2	1.60	−20.54	10.86	10.34	−12.27	0.60	<7.97	<−2.89
2530	23 24 23.50	15 26 36.30	2MASX J23242356+1526362	7658 ± 2	1.49	−19.70	10.41	9.96	−11.86	0.60	<7.94	<−2.47
2535	23 25 33.60	14 15 15.00	ASK 144275	3783 ± 5	0.88	−15.72	8.39	8.36	−10.55	0.60	<7.36	<−1.03
2584	23 52 36.40	14 33 05.20	UGC 12822	7939 ± 2	1.50	−21.37	11.04	10.62	−12.03	0.71	<8.07	<−2.97

Notes. Flags in Col. 1: *C* for targets clearly confused with another galaxy within the Arecibo telescope beam, *M* for marginal Nançay detections, and *U* for unreliable photometry.